



## Coseismic landslides triggered by the 2022 Luding Ms6.8 earthquake, China

**Abstract** On September 5, 2022, an Ms6.8 earthquake struck Luding County, Sichuan Province, China. Through creating a coseismic landslide prediction model, we obtained the spatial distribution of the triggered geological hazards immediately after the earthquake. Through collecting all available multi-source optical remote sensing images of the earthquake-affected area via UAV and satellite platforms, the exact information of coseismic landslide was achieved by pattern recognition and visual inspection. According to the current results, the Luding earthquake triggered 5336 landslides with a total area of 28.53 km<sup>2</sup>. The spatial distribution of the coseismic landslides is correlated statistically to various seismic, terrain, and geological factors, to evaluate their susceptibility at regional scale and to identify the most typical characteristics of these failures. The results reveal that the coseismic landslides mainly occurred on the sides of the Xianshuuhe fault (within 1.2 km) and Dadu River (within 0.5 km) in striped patterns. They are concentrated in the regions with an elevation range of 1000–1800 m, a slope range of 25–55°, and lithologies of acid plutonic rocks, mixed sedimentary rocks, and siliciclastic sedimentary rocks. Besides, the coseismic landslides of the Luding earthquake are smaller in size and shallower than those triggered by the 2008 Wenchuan earthquake and the 2017 Jiuzhaigou earthquake. Rapidly achieving the spatial locations and distribution patterns of the coseismic landslides enables to provide effective support and guidance to emergency rescue, risk mitigation, and reconstruction planning.

**Keywords** Coseismic landslides · Luding earthquake · Prediction · Remote sensing · Interpretation · Spatial distribution

### Introduction

On September 5, 2022, an Ms6.8 earthquake with the epicenter of 29.59°N, 102.08°E, and a focal depth of 16 km jolted Luding County, Sichuan Province, China. The seismic shaking lasted for 20 s, and 2715 aftershocks were subsequently recorded. The earthquake was acutely felt in many western provinces, including the metropolis of Chengdu, Chongqing, and Xi'an, about 226 km, 444 km, and 830 km away from the epicenter, respectively. According to the shaking intensity map (the [Ministry of Emergency Management releases intensity map of Luding magnitude 6.8 earthquake in Sichuan Province — Ministry of Emergency Management, PRC](#), in Chinese) announced by the Ministry of Emergency Management of China, which is based on a modified Mercalli (MM) scale (GB/T 17,742–2020, 2020), the area with seismic intensity larger than VI degree is 19,089 km<sup>2</sup>, and the maximum intensity reaches IX degree with an area of 280 km<sup>2</sup> (An et al. 2022). The earthquake triggered a large number of coseismic landslides, damaged houses, and blocked

roads in the affected area, resulting in severe casualties and property losses. According to statistics, it has caused 93 fatalities and 25 people missing until September 12, 2022.

Such strong earthquake usually triggers extensive geological hazards, including landslides, debris flows, and rock avalanches, and has a long-term modification on the landscape and environment in mountainous regions (Fan et al. 2019; Kincey et al. 2021; Tang et al. 2011). These geological hazards, together with postseismic rainfalls, concur to pose severe threats to the local community (Budimir et al. 2014; Yin et al. 2009). Thus, rapid and accurate identification of the location of coseismic geohazards is critical for risk mitigation and future reconstruction in the earthquake-affected region (Williams et al. 2018; Xu et al. 2012). Furthermore, documentation of the detailed inventories for coseismic geohazard events is significant for future studies on the evolution of the landscape in this region (Fan et al. 2021; Galli et al. 2008; Guzzetti et al. 2012). Earth observations from remote sensing images, which are provided with large area coverage but short revisit times, offer a great opportunity of monitoring land surface process in wide geographical areas compared to time and labor costly in situ investigation (Lee 2005; Roy et al. 2014). On this basis, coseismic landslide mapping based on remote sensing technology has been developed rapidly and has become the most important means of achieving their distributions and patterns (Mantovani et al. 1996; Van Westen et al. 2008). At present, the machine learning-based classifier became the popular way of large-scale automatic landslide detection. However, landslides usually occur in mountainous areas with complicated terrains, leading to certain mapping differences through various classifiers with sophisticated pixel value distribution in remote sensing images (Reichenbach et al. 2018). Hence, an effective classifier for a research area may not be satisfactory to another study case (Wang et al. 2022; Woźniak et al. 2014).

Detailed coseismic landslide maps are usually produced by on-site investigation or interpreting the optical remote sensing images obtained from satellites, unmanned aerial vehicles (UAVs), or helicopters (Galli et al. 2008; Guzzetti et al. 2012; Hovius et al. 1997; Rossi et al. 2018). However, effective satellite images are often limited by weather conditions. In addition, field conditions are also difficult to meet the standard of on-site investigation and UAV/helicopter mission. Therefore, coseismic landslide prediction is of great significance for the guidance and decision-making of emergency rescue during the period without post-earthquake images and investigations. The current methods for coseismic landslide prediction based on statistical analysis, such as logistic regression, linear regression, and support vector machine, are widely used in many researches (Guzzetti et al. 2006), which provide relative

## Recent Landslides

estimate of landslide spatial occurrence based on various conditioning factors (Brenning 2005; Budimir et al. 2015; Lee et al. 2008; Tanyas et al. 2019). However, the current methods generally have the following limitations: (1) these data-driven models do not contain rich enough samples of historical earthquake-induced landslides. (2) The controlling factors of the landslides are unclear, leading to insufficient consideration of learning features. (3) The linear or nonlinear intelligent algorithm based on machine learning cannot fully explore the comprehensive correlation between the triggered landslides and the controlling factors.

In view of the mentioned problems existing in the mapping and prediction, and the urgent need of rapid and accurate inventory for emergency rescue after a sudden hazard, a comprehensive framework of evaluating the triggered landslides after a strong earthquake is proposed in this paper, in which the 2022 Luding earthquake is adopted as a typical case. First, a novel coseismic landslide prediction model is carried out based on global landslide samples and deep learning algorithms to immediately achieve the landslide distribution. Then, landslide mapping based on the strategy of ensemble learning will be performed once post-earthquake remote sensing images are acquired. Last but not least, with the integration of coseismic landslide prediction and interpretation, this work is aimed at providing a detailed landslide inventory and at delivering a quick statistical evaluation of the spatial distribution and controlling factors of the geological hazards induced by the 2022 Luding earthquake, with the twofold scope of providing a first-hand information for the risk assessment related to possible

secondary geohazards and of supporting the guidance for post-earthquake reconstruction and planning.

### Study area

The 2022 Luding earthquake is located in the Hengduan Mountains, the southeastern margin of the Qinghai-Tibet Plateau, which is a typical alpine canyon landform. The Dadu River runs through the area from north to south with a huge river drop. The dominant lithologies of the interior layers in this region are the acid plutonic rocks and mixed sedimentary rocks. Due to the long-term effect of strong tectonic action and weathering, the rock and soil mass is quite broken, providing favorable conditions for the occurrence of geological hazards. The earthquake occurred near the Moxi fault in the southeastern segment of Xianshuihe Fault with a direction of NW–SE.

As the strike-slip boundary between the Bayan Har block and the Sichuan–Yunnan block, the Xianshuihe Fault is one of the most active faults in China, forming the famous Y-shaped fault zone with the Longmenshan Fault and the Anninghe Fault (Fig. 1). The Xianshuihe Fault is a left-lateral strike-slip fault about 350 km long, starting from Donggu town (Ganzi county) in the north and extending to Tianwan town (Shimian county) in the south via Luhuo, Daofu, Qianning, and Kangding counties. The Xianshuihe Fault consists of five major branching faults, and their long-term slip rates are remarkably different among the north and south segments. Specifically, the slip rate in the north of the Qianning segment is 14~20 mm/a, whereas it is 9.6~13.4 mm/a for the Moxi segment (Bai et al. 2018, 2021; Chen et al. 2016). As a result, different

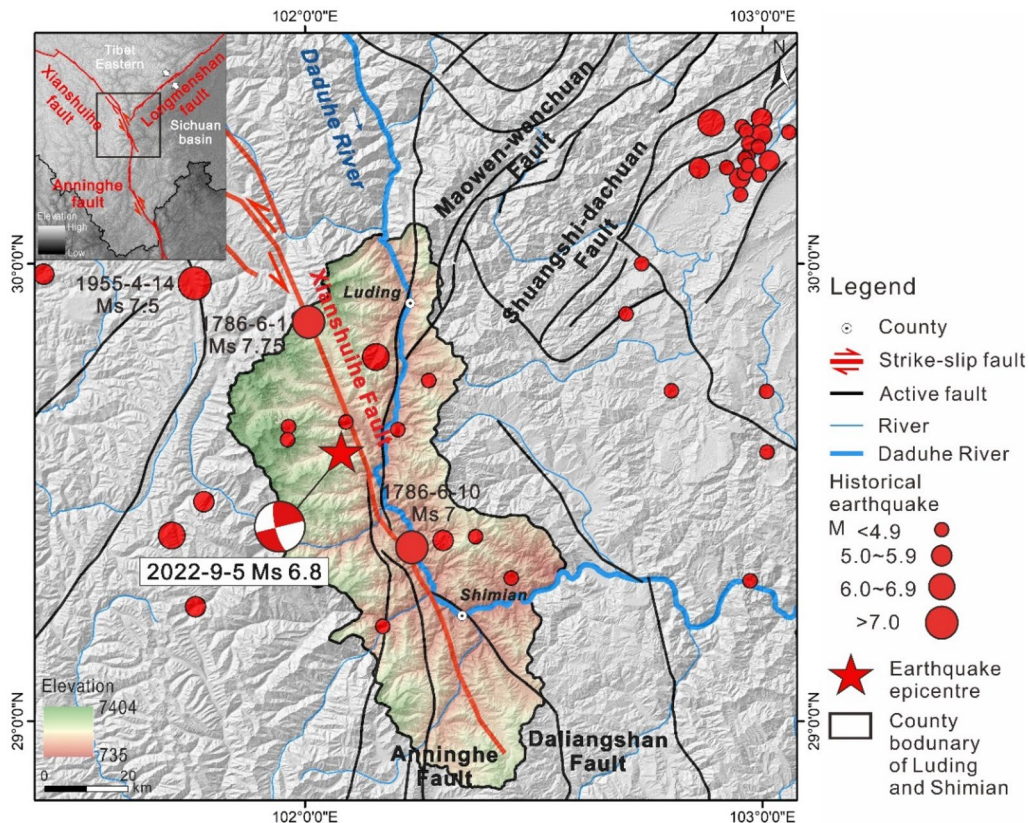


**Fig. 1** The epicenter and major faults related to the 2022 Luding Ms6.8 earthquake

behaviors on intensity and frequency of seismic activities are observed in different segments of the Xianshuihe Fault. The Luding earthquake is most probably induced by the seismic activity of Moxi segment in the Xianshuihe Fault.

The Xianshuihe Fault has experienced several strong seismic activities in history, including nine  $M_s \geq 7.0$  earthquakes since 1700. The most famous earthquake is the 1786 Kangding-Moxi  $M_s 7.75$  earthquake, which is also spatially closest to the Luding earthquake epicenter. The most recent seismic activity in this area is the 1973 Luhuo  $M_s 7.6$  earthquake. It is worth mentioning that the Coulomb stress near Xianshuihe Fault increased significantly after the 2008 Wenchuan  $M_s 8.0$  earthquake and the 2013 Lushan  $M_s 7.0$  earthquake occurred on the Longmenshan Fault. The strike-slip rate has been increasing from northwest to southeast, indicating a possibility of inducing this large earthquake in the Xianshuihe Fault.

### Coseismic landslide prediction

Rapid estimation of spatial distributions and controlling factors of coseismic landslides are essential for emergency rescue after an earthquake. Based on the global dataset, a near-real-time prediction model of earthquake-triggered landslide was established via the machine learning algorithm (Fan et al. 2022). It is worth noting that the dataset contains 90,655 coseismic landslide samples of the recent seismic events that occurred in the Alpine canyon zone of the Tibetan Plateau periphery, including the 2021 Luxian  $M_s 5.9$  earthquake, the 2022 Menyuan  $M_s 7.1$  earthquake, and the 2013 Lushan  $M_s 6.1$  earthquake. Ten controlling factors were selected and adopted as the input features through information gain (Fan et al. 2021). In terms of topography and landform, four characteristics including elevation, slope, aspect, and curvature were considered. The lithology and fault distance were extracted as important geological structure controlling factors of landslide development. Land cover type and distance from rivers were also considered as key influencing factors for the geological environment. Meanwhile, the peak ground motion acceleration (PGA) and peak ground motion velocity (PGV) were selected as the trigger factors of coseismic landslide (Fan et al. 2022). The characteristics used are listed in Table 1. The coordinate system of these data was standardized and

unified as the WGS 1984 geographic coordinate system for global model construction. Deep forest (DF) is a new tree-based deep learning method, which is different from deep neural network based on the neurons structure. By integrating and connecting the forests which composed of trees, it enables to achieve the purpose of making the classifier do the representational learning, greatly improving the classification result (Lyu et al. 2017). Through comparisons of cross-validation for the current popular algorithms including random forest, extreme gradient boosting, multilayer perceptron, and convolutional neural network, DF was adopted to construct the prediction model thanks to its better performance. It has already been successfully applied in coseismic landslide prediction in the southeastern margin of the Qinghai-Tibetan Plateau (Fan et al. 2022; Zhou and Feng 2019). The detailed parameters for the prediction model are available (Fang 2023).

We applied the model immediately after the Luding earthquake, and achieved the corresponding triggered landslides (Fig. 2). Note that for the subsequent research of Luding earthquake-triggered landslides, all the data were uniformly converted into a projected coordinate system of WGS 1984 UTM Zone 48N to facilitate spatial matching and statistical analysis. The coseismic landslide area with very high probability is  $20.71 \text{ km}^2$ , accounting for 0.16% of the total considered area. The areas with high and medium probabilities are  $142.39 \text{ km}^2$  and  $401.29 \text{ km}^2$ , respectively, accounting for 1.1% and 3.1% of the total considered area. The areas with low and very low probabilities are  $1809.75 \text{ km}^2$  and  $10,570.96 \text{ km}^2$ , respectively, accounting for 13.98% and 81.66% of the total considered area. To quantitatively analyze the accuracy of the prediction, the visual interpretation of coseismic landslides based on remote sensing images were used for evaluation. The results are in good agreement with the actual landslide locations. Their overall accuracy and the Kappa coefficient, which is an index for measuring inter-rater reliability for categorical results, are 77.24% and 0.54, respectively. The area under the ROC curve (AUC), which is also an important evaluation metric for checking the performance of a prediction model, reaches 0.84 (Fig. 3). These indicators confirm the effectiveness and reliability of the prediction for the Luding earthquake-triggered landslides.

**Table 1** General description of conditioning factors adopted in this paper

| Class      | Factors           | Data source                                   | Resolution/<br>scale |
|------------|-------------------|---|----------------------|
| Topography | Elevation         | Elevation taken directly from NASA SRTMS DEMS | 30 m                 |
|            | Slope             | Slope angle derived from NASA SRTMS DEMS      |                      |
|            | Aspect            | Aspect derived from NASA SRTMS DEMS           |                      |
|            | Curvature         | Curvature derived from NASA SRTMS DEMS        |                      |
| Lithology  | Lithology         | Global Lithology Map                          | 1:200,000            |
|            | Distance to fault |   |                      |
| Seismicity | PGA               | USGS ShakeMap System                          | 1000 m               |
|            | PGV               |   |                      |
| Climate    | Land use          | GlobeLand30                                   | 30 m                 |
|            | Distance to river |   |                      |

## Recent Landslides

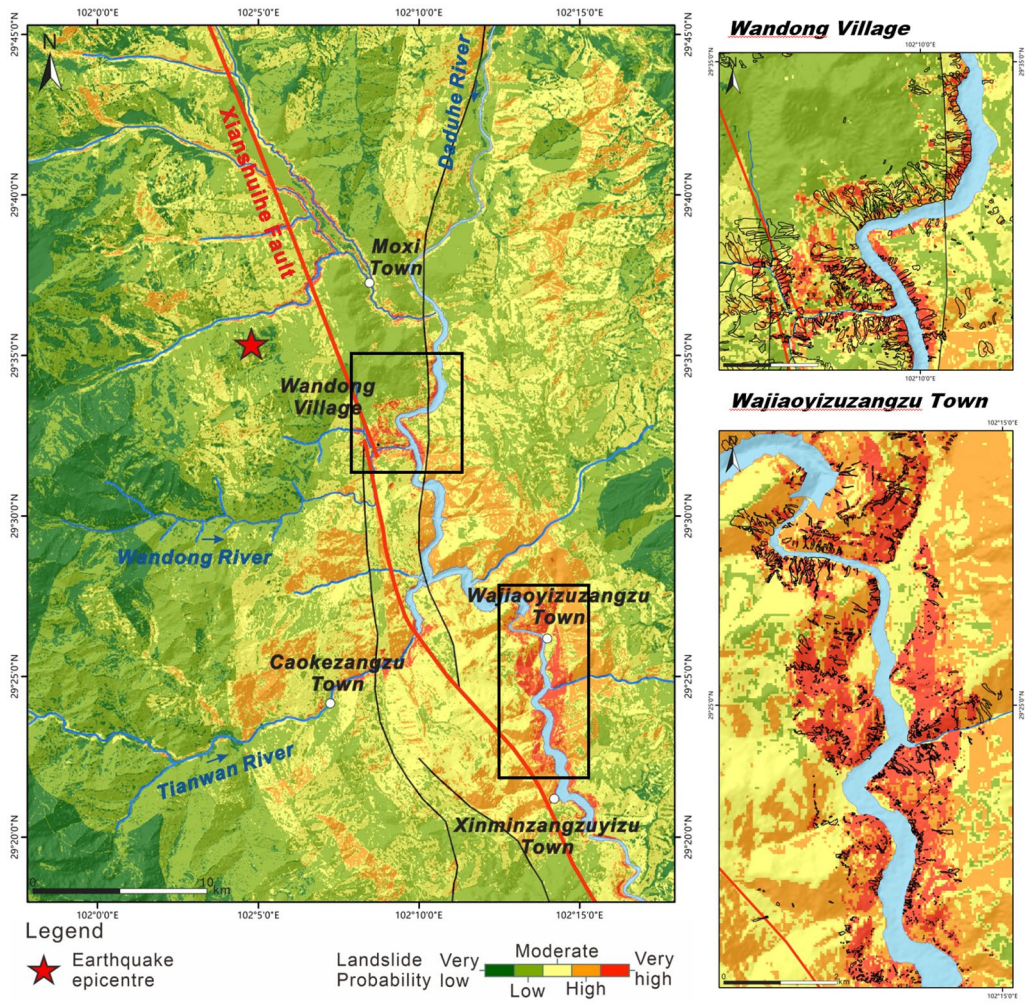


**Fig. 2** Prediction of spatial distribution probability of the **a** Luding earthquake-triggered landslides and examples of interpreted landslides at **b** Wandong Village and **c** Wajiao Town

### Coseismic landslide interpretation

To figure out the actual spatial distribution of coseismic landslides, we rapidly collected remote sensing images through different data sources after the earthquake, which mainly include UAV- and satellite-based images. Due to the following cloudy and rainy weather, it was difficult for optical image acquisition via satellite platforms to cover the entire earthquake-affected area in a short time, making it difficult to realize landslide recognition based on change detection approach through images before and after the earthquake. With continuous efforts and multiple data sources, we finally achieved a high-resolution composite image with less cloud cover through multi-temporal images. Compared to change detection, classification-based algorithm enables to realize more rapid, automatic, and accurate landslide identification under such data conditions. Subsequently, experienced experts in geological interpretation eliminated the identified pre-earthquake landslides (false detection) according to the comparison between pre- and post-earthquake images through visual inspection, obtaining the final results. The information of available images is displayed in Fig. 4.

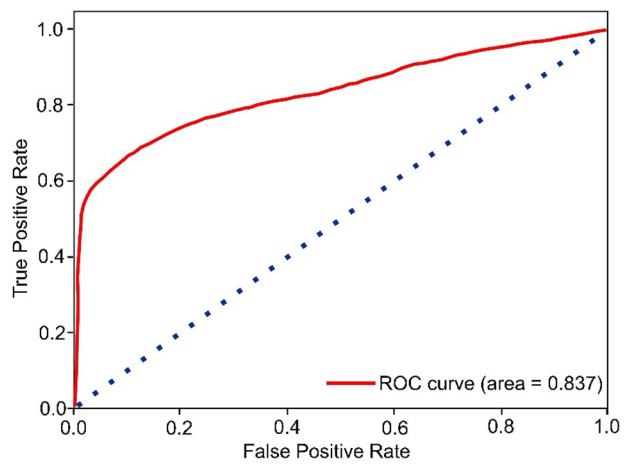


**Fig. 3** ROC of the prediction results

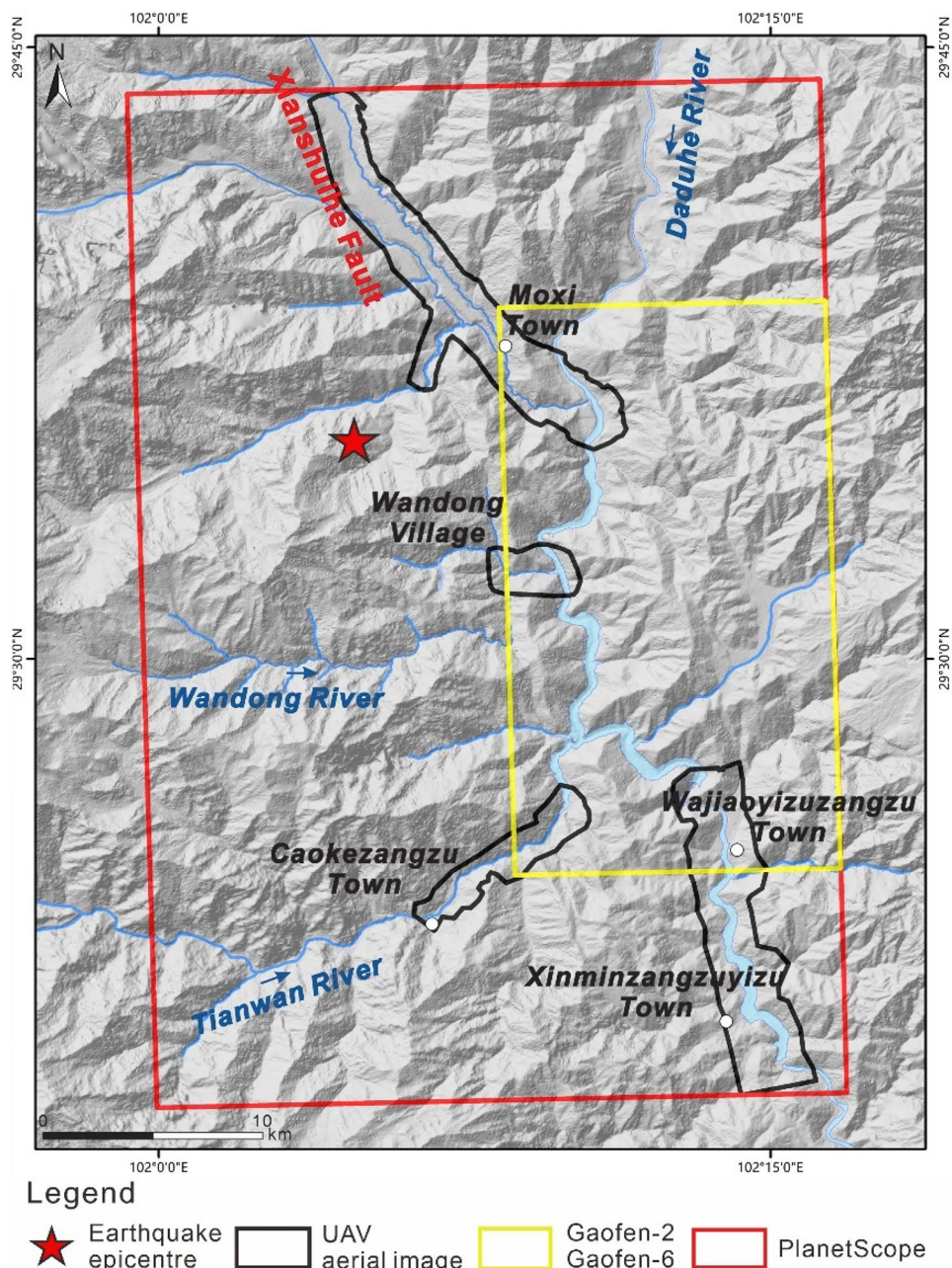
## UAV-based image interpretation

Due to the cloudy weather, satellite-based optical images were difficult to be utilized after the earthquake. We took the lead in carrying out UAV missions and successively acquired five remote sensing images (with spatial resolutions of 0.15–0.2 m) of the severely affected areas. To ensure data standardization and model generalization, their spatial resolutions and data types were normalized to 0.2 m and uint8, respectively. Finally, the sliding window was used to crop the remote sensing image into the patches with the size of 512×512 pixel for further model input.

To serve emergency relief, we first adopted SegFormer, which is a semantic segmentation model based on Transformer, to

automatically detect coseismic landslides as soon as possible (Dosovitskiy et al. 2020). It has already performed well in the 2017 Jiuzhaigou earthquake-triggered landslide detection (Tang et al. 2022). SegFormer consists of an encoder and a decoder (Xie et al. 2021). The encoder is used to extract landslide features from UAV images automatically, and the input of the encoder is small image patches with a size of 512×512×3. The encoder consists of four transformer blocks with different sizes. Transformer captures global dependencies among the image elements, which significantly improves the reception field of SegFormer. A CNN-based position embedding block is used to learn geo-position information of the image elements. The output of SegFormer is a feature map with a size of 16×16×2048. The decoder is used to decide whether each

**Fig. 4** Remote sensing image coverage in the Luding earthquake-affected area



## Recent Landslides

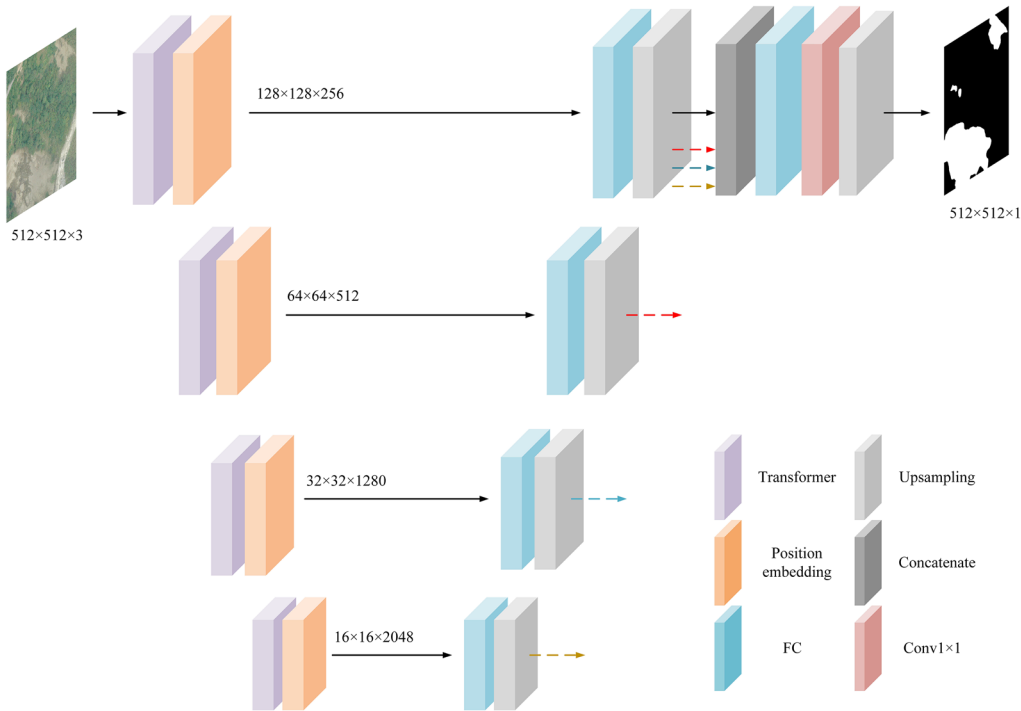


**Fig. 5** The architecture of SegFormer

image element belongs to the range of landslides, and the input of the decoder is four hierarchical feature maps. To improve the semantics of low-resolution feature maps and the details of high-resolution feature maps, SegFormer fuses the hierarchical feature maps. Specifically, the upsampling operation is employed to expand low-resolution feature maps to  $128 \times 128$ . The concatenate operation is employed to merge all the feature map into a unified feature map with a size of  $128 \times 128 \times 768$ . Finally, a fully connected layer, a convolution layer, and an upsampling layer are used to predict the class label of each image element. The architecture of the SegFormer-based approach is displayed in Fig. 5. The detailed parameters for the model are available (Liu et al. 2021).

To evaluate its recognition performances, we manually interpreted the earthquake-triggered landslides in Caoke and Moxi towns. The former was adopted as training samples, whereas the latter was used as test samples. Thus, the training and test dataset are collected from two different areas without any overlap. The UAV images are divided into small patches. The dividing method is a sliding window without an intersection. Thus, there are 4125 training samples and 1350 test samples. The train/test ratio is about 3:1. Supervised semantic segmentation requires accurate landslide labels. We manually annotate all the landslides in the image patches. The hyperparameter configurations are shown as follows. The version of SegFormer is B4. AdamW is adopted as the optimization algorithm (Loshchilov and Hutter 2017). The initial learning rate and weight decay factor are set as 0.00006 and 0.01. The batch size and the numbers of iteration are set as 4 and 8000, respectively. We use mean interaction over union (mIoU), F1 value, precision, and recall to make the assessments, which are listed in Table 2. It can be seen that the average IoU and F1 value reach 0.844 and 0.864. For coseismic landslides, the IoU and F1 values of the coseismic

landslide are 0.71 and 0.83, respectively. At the same time, all the evaluation metrics of the background are greater than or equal to 0.977. Therefore, the SegFormer-based approach enables to achieve good performances for both coseismic landslides and background classes in this event. The coseismic landslide detection results via the SegFormer-based approach are shown in Fig. 6.

### Satellite-based image interpretation

On September 10, 5 days after the earthquake, we obtained satellite-based image of the influenced area from the cloud gap through Gaofen-6. Co-registration is implemented to ensure that image pixels or objects of panchromatic and multispectral (including blue, green, red, and near-infrared bands) images in the same location are comparable. To ensure high accuracy of matching, the images are co-registered to a root-mean-square error of less than 0.5 pixels. Gram-Schmidt pan-sharpening is then adopted to improve the spatial resolution of Gaofen-6 imagery, achieving a 2-m resolution fusion image. Affected by the weather after the earthquake, the land cover information was blocked by clouds in most parts. Fortunately,

**Table 2** Accuracy assessment of coseismic detection in Moxi town via SegFormer-based approach

| Class      | IoU   | Precision | Recall | F1 value |
|------------|-------|-----------|--------|----------|
| Landslide  | 0.710 | 0.865     | 0.798  | 0.830    |
| Background | 0.977 | 0.986     | 0.991  | 0.988    |
| Average    | 0.844 | 0.925     | 0.894  | 0.864    |

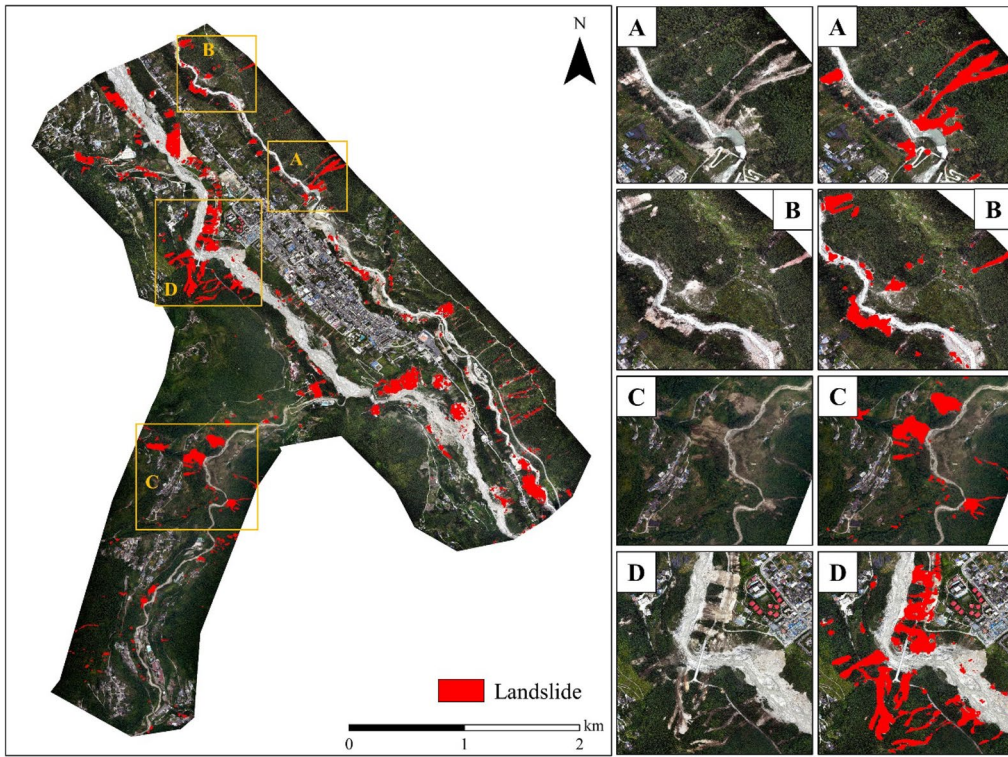


**Fig. 6** Coseismic landslide detection in Moxi town via SegFormer-based approach

the hardest hit area by geological hazards happened to be displayed through an empty window, where the situation of the land surface can be investigated. We obtained a range covering around  $312\text{km}^2$ , which mainly contains five types of targets, including landslide, vegetation, water, impervious surface area (ISA), and cloud/cloud shadow. We adopted the methods of feature extraction and model construction as Wang et al. (2022), whose effectiveness has been proved in multiple recent case studies of earthquake-triggered landslide recognition. Thus, we constructed multi-scale extended morphological profiles (EMPs) after principal component analysis (PCA) transformation of the fused Gaofen-6 images (Benediktsson et al. 2005; Dalla Mura et al. 2011). According to the experiences, the scale parameter of EMPs was defined as [2,3]. The classification-based interpretation model integrated K-nearest neighbor (KNN), support vector machine (Mountrakis et al. 2011), random forest (Belgiu and Drăguț 2016), and rotation forest (Rodriguez et al. 2006), whose parameters were set the same as Wang et al. (2022).

Before acquiring satellite remote sensing images, we obtained some coseismic landslide information by means of intelligent identification and visual interpretation through aerial UAV images of several small areas within the range. These landslide data were resampled to the same spatial resolution as Gaofen-6 with a total number of 231,618 pixels, of which 2% are selected as training samples, and the remaining 98% are used as test samples for performance evaluation. At the same time, the other four categories of targets in the image were visually interpreted. The same number of pixels were selected for each category to integrate with the landslide training samples to construct a training set, whereas the remainder were

integrated with the landslide test samples to construct a testing set. Table 3 lists the confusion matrix of the classification result. The overall accuracy reached 94.37%, and the Kappa coefficient was 0.9145, which indicate that the targets contained in the image could be effectively recognized. In particular, for the coseismic landslides, the producer accuracy reaches 83.46%, and the user accuracy reaches 78.38%. The results show that this approach realized high accuracy for the identification of coseismic landslides, and its reliability is further validated in the rapid and intelligent identification of large-scale geological hazards after a strong earthquake. Figure 7 displays the Gaofen-6 image and the corresponding classification result.

#### Comprehensive results of the coseismic landslides

To obtain comprehensive coseismic landslides, we continued to pay attention to multi-source satellite-based images after the earthquake. Finally, through the PlanetScope images on September 29 and October 1–3, a synthesized optical image covering almost the entire earthquake-affected area was achieved. We resampled the land cover results from UAV and Gaofen-6 images to 3-m resolution, which is consistent with the PlanetScope data. For each class, 2000 pixels are selected as training samples to extract multi-scale EMPs (the training samples of cloud class were directly selected from PlanetScope images) to train the ensemble learning-based model. The entire image was then classified, and the landslides were selected from the classification

## Recent Landslides

**Table 3.** Confusion matrix based on the results of Gaofen-6 image

Table.3 Confusion matrix based on the results of Gaofen-6 image

| Class           | Landslide | Vegetation | Water | ISA   | Cloud | Producer accuracy/% |
|-----------------|-----------|------------|-------|-------|-------|---------------------|
| Landslide       | 10026     | 5          | 6     | 1853  | 123   | 83.46               |
| Vegetation      | 16        | 51260      | 106   | 52    | 204   | 99.27               |
| Water           | 653       | 1          | 11197 | 67    | 0     | 93.95               |
| ISA             | 1955      | 36         | 20    | 8981  | 115   | 80.86               |
| Cloud           | 141       | 57         | 1     | 179   | 12271 | 97.01               |
| User accuracy/% | 78.38     | 99.81      | 98.83 | 80.68 | 96.52 | 94.37               |

result. Finally, the final interpretation of the Luding earthquake-triggered landslides were obtained by visual inspection of the landslide type classified.

Figure 8 shows the composite image and the corresponding identification results of coseismic landslides. The image covers  $1258\text{km}^2$  of the earthquake-affected region, and the total area of coseismic landslide detected reaches  $28.53\text{km}^2$  (including 5336

landslides), accounting for 3.27% of the available image pixels. The slopes near the Xianshuihe Fault and Dadu River (including its tributaries) are the regions where geological hazards are concentrated. The number and density of earthquake-triggered landslides in the Wandonghe basin, east of Detuo town, is the highest all over the region. Large-scale continuous landslides occurred on both sides of the Xianshuihe Fault within Detuo and Tianwan

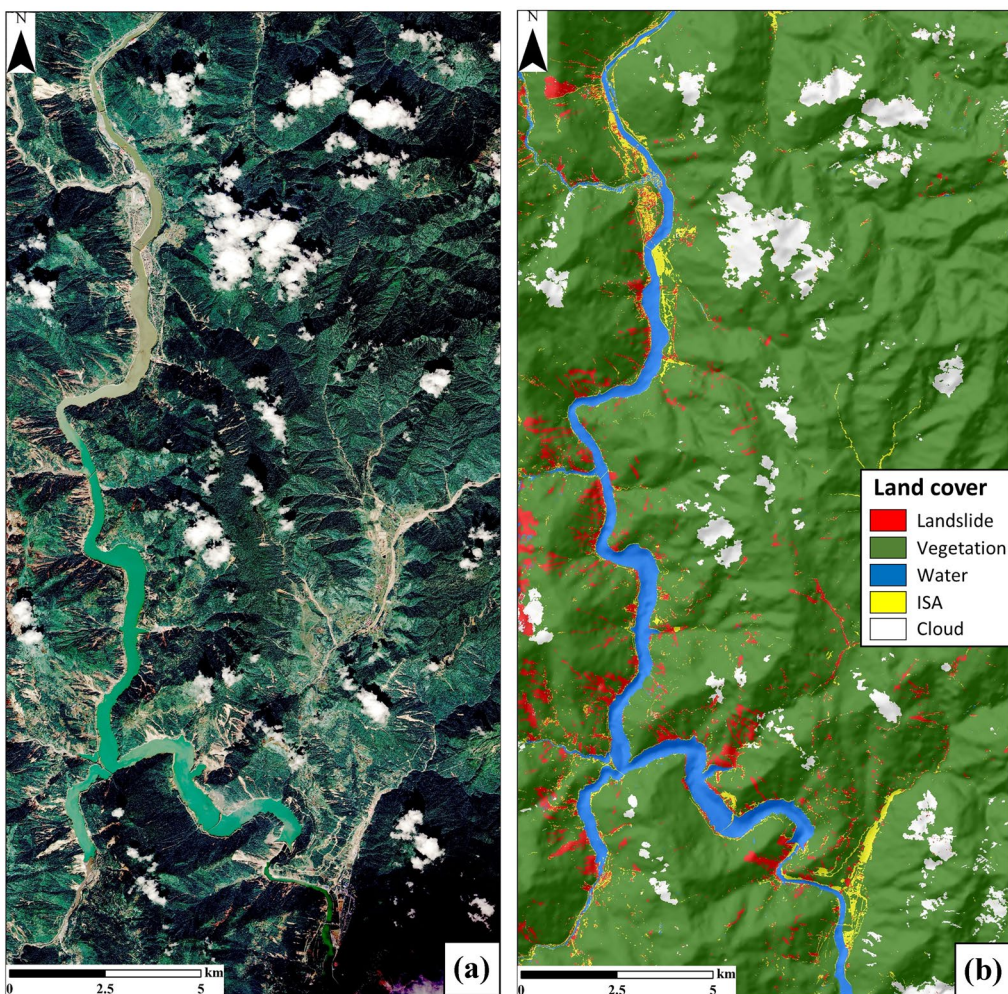


**Fig. 7** **a** Gaofen-6 remote sensing image and **b** the corresponding land cover classification

towns, and the average area of a single landslide is the largest in the earthquake-affected zone. The slope bodies on both sides of the Tianwan River in Caoke town are another concentration area of coseismic landslides triggered. In addition, many landslides, whose areas are small, also occurred along both sides of the Dadu River in Wajiao town. According to the on-site investigation, the geological hazards caused by the earthquake caused serious damages to the urban infrastructure and traffic arteries. Under the influence of rainfall and construction after the earthquake, the main roads in the towns have experienced landslides destroyed and emergency repairs several times.

#### Spatial distribution of the coseismic landslides

The epicenter of the Luding earthquake is located at the confluence of three major faults. The effects of strong tectonic movement and deep river valley unloading resulted in great the development of rock mass joints and fractures in this area. Therefore, under the action of strong ground movement, it is easy to trigger collapse and landslide hazards, which are mainly concentrated in the IX and VIII degree intensity area along the Xianshuihe Fault (Fig. 9). A large number of small-sized landslides are concentrated in Moxi platform, the Wandonghe basin, Wajiao town, and the banks of the Dadu river, around the Moxi platform. These landslides are shallow and have little impact on the Dadu river. The Wandong village is located in the center of the IX intensity area, where the coseismic landslide scale is the largest and densely developed at the mouth of the ditch. However, the coseismic landslides are numerous on a small scale in Wajiao town. The extensive coseismic landslides led to a large area of buried road and damaged roadbeds in mountainous areas, seriously affecting the emergency rescue. Moreover, many houses were directly destroyed, especially in Mogangling and Wandong villages, leading to serious casualties.

Seismic, topography, and geologic factors are generally considered the main factors that contribute to the spatial distribution of coseismic landslides (Fan et al. 2018; Keefer 1984, 2000; Nowicki

Jessee et al. 2018). To identify the most relevant factors controlling the coseismic landslides of this event, ten factors, including distance to seismogenic fault, distance to closest fault, distance to the epicenter, PGA, elevation, slope, aspect, distance to river, distance to road, and lithology, were taken into account. The distribution of landslides area and areal density for each factor were both statistically analyzed.

#### Seismic factors

According to the seismogenic mechanism, more intense shaking is likely to happen close to the seismogenic fault and is easier to trigger coseismic landslides. The seismogenic fault of this earthquake is the Moxi section of the Xianshuihe Fault, which is a sinistral strike-slip fault with NW–SE direction. Most of the coseismic landslides (62%) were observed within 5 km away from the seismogenic fault, and the landslide area shows a decreasing trend with the increasing distance to the seismogenic fault (Fig. 10a). The landslide distribution on both sides of the seismogenic fault is slightly different. In detail, 54.4% of the coseismic landslides occurred on the southwest side of the seismogenic fault, while 45.6% occurred on the northeast side. The correlation between landslide occurrence and the distance to the closest geologic faults was also investigated (Fig. 10b). The results show that 54.8% of the total landslides are distributed less than 2 km away from the closest fault. In particular, 39.6% are within a distance of 1 km.

The epicenter does not have an obvious impact on the coseismic landslide distribution as observed in other earthquake events (Bao et al. 2019; Valagussa et al. 2019; Wang et al. 2019), which is probably due to incomplete observations so far. In detail, nearly 96% of the coseismic landslides distributed within the radius of 9–27 km away from the epicenter, whereas less than 1% of the landslides occurred within 3 km (Fig. 10c). Figure 10d displays the relationship between PGA and the coseismic landslide distribution. The results show that

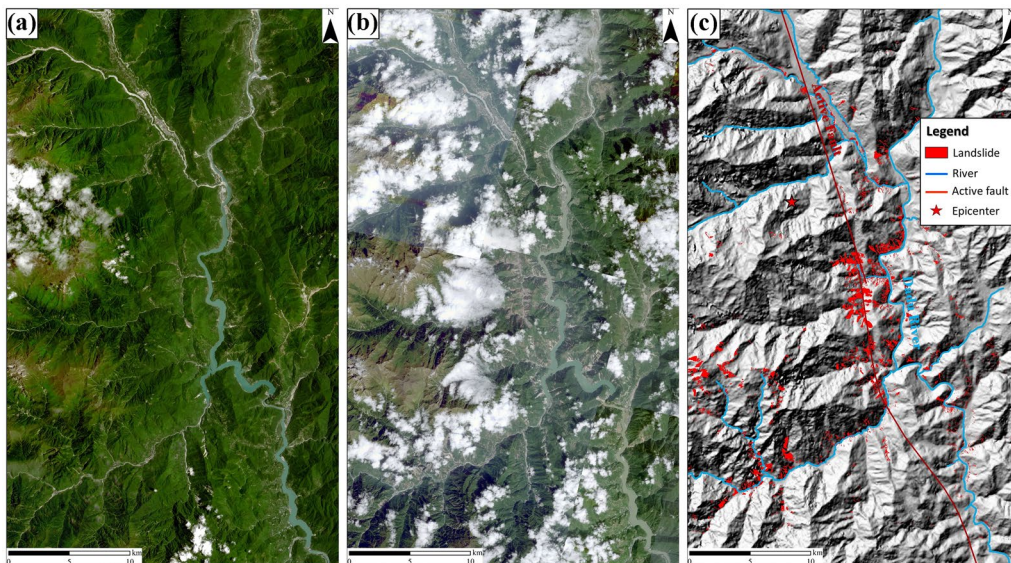
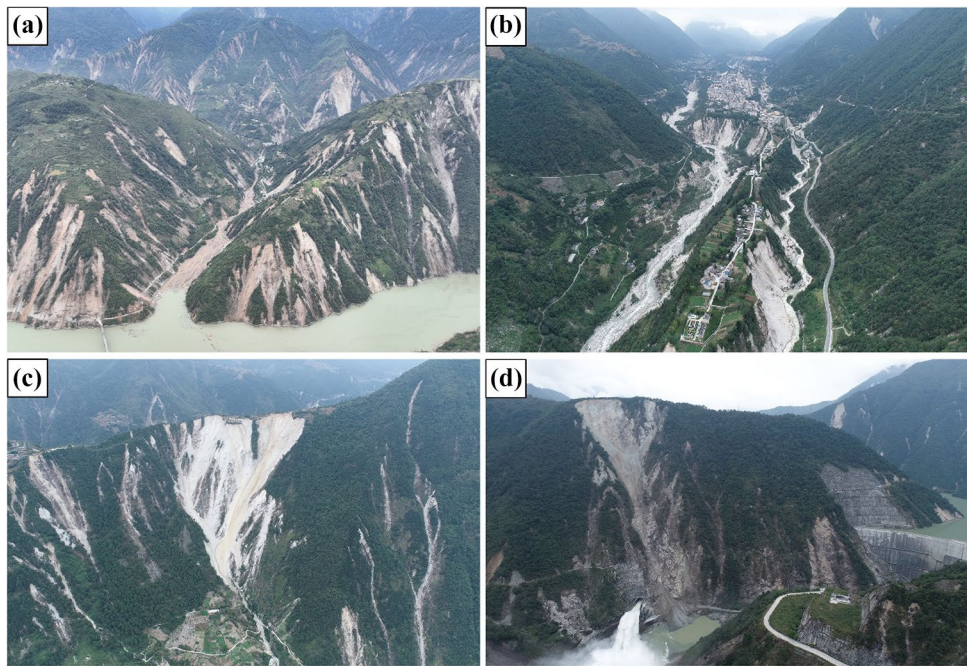


**Fig. 8** PlanetScope remote sensing image before (a) and after (b) the Luding earthquake, and the corresponding interpretation of earthquake-triggered landslides (c)

## Recent Landslides

**Fig. 9** The aerial photos of the coseismic landslides in the area: **a** landslides in Wandong village; **b** landslides on Moxi platform; **c** Mogangling landslide; **d** landslides over the Dagangshan hydropower station



$\text{PGA} = 0.3 \text{ g}$  is the minimum threshold of the coseismic landslides in the 2022 Luding earthquake. The landslide area and areal density both reach the peak when PGA is in the range of 0.5–0.6 g, followed by 0.7–0.8 g. Higher PGA does not completely match larger landslide area or areal density, indicating that the landslides were triggered by a compound effect of multiple factors.

### Terrain factors

To elucidate the influence of terrain factors on earthquake-induced landslides, the elevation, slope, and aspect were extracted via geographic information system (GIS) analysis by using digital elevation model from NASA with a spatial resolution of 30 m (Crippen

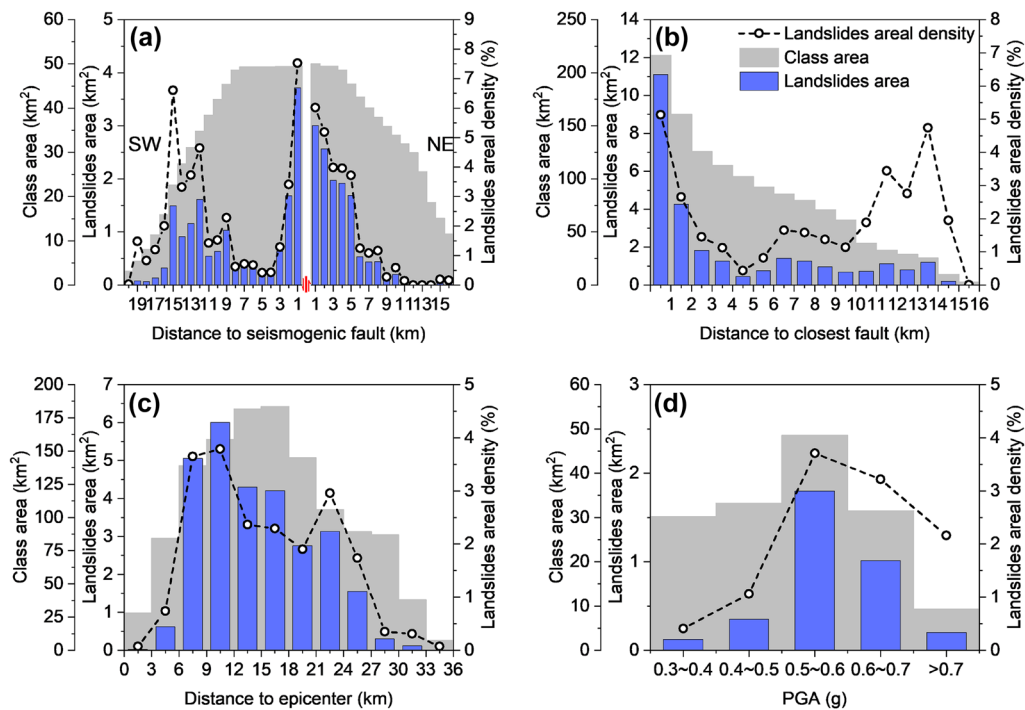


**Fig. 10** Relationship between coseismic landslide distribution and seismic factors: **a** distance to seismogenic fault, **b** distance to closest fault, **c** distance to epicenter, and **d** PGA

et al. 2016). They were then resampled to 3-m resolution to match the landslide interpretation results for subsequent analysis.

As a result, the elevation of the earthquake-affected area ranges from 800 to 5000 m. The landslide area increases with the growth of elevation until 1600 m and then decreases until 3000 m conversely (Fig. 11a). After that, the landslide areas were maintained at low levels. The elevation of 1000–2400 m contains 22.2 km<sup>2</sup> of landslides, occupying 78.3% of the total landslide area. This result indicates that the coseismic landslides tend to occur in the valley at low elevations. As is shown in Fig. 11d, the closer to rivers, the greater the coseismic landslide area is. The landslide area within 500 m away from rivers accounts for 64.7% of the total. With slope angle growth, the landslide area first increases and then decreases (Fig. 11b). The angles between 25 to 55° aggregate 23.2 km<sup>2</sup> landslides, accounting for 81.7% of the total landslide area. In terms of the slope aspect, it reveals that the coseismic landslides are mainly developed on the aspects of E and SE, accounting for 44.8% of the total coseismic landslide area, followed by NE and S (26.6% in total) (Fig. 11c). It seems that there is no obvious relationship between the

aspect of the coseismic landslides and the strike of the seismogenic fault in this event.

Figure 11e presents a negative correlation between the coseismic landslide distribution and the distance to roads, which might indicate the promotion of facilities construction to coseismic landslides. However, these roads in mountainous areas are usually built along rivers, which make it difficult to distinguish their independent impacts of rivers and roads on the coseismic landslides triggered.

### Lithological factors

To reveal the distribution of earthquake-induced landslides in different lithologies in detail, the lithology data were acquired from global lithological map (Hartmann and Moosdorf 2012) and converted from vector to raster data format with a spatial resolution of 3 m, which is consistent to the interpretation achievements and beneficial to subsequent statistical analysis. It is worth noting that a target pixel may contain vectors with multiple attributes in data

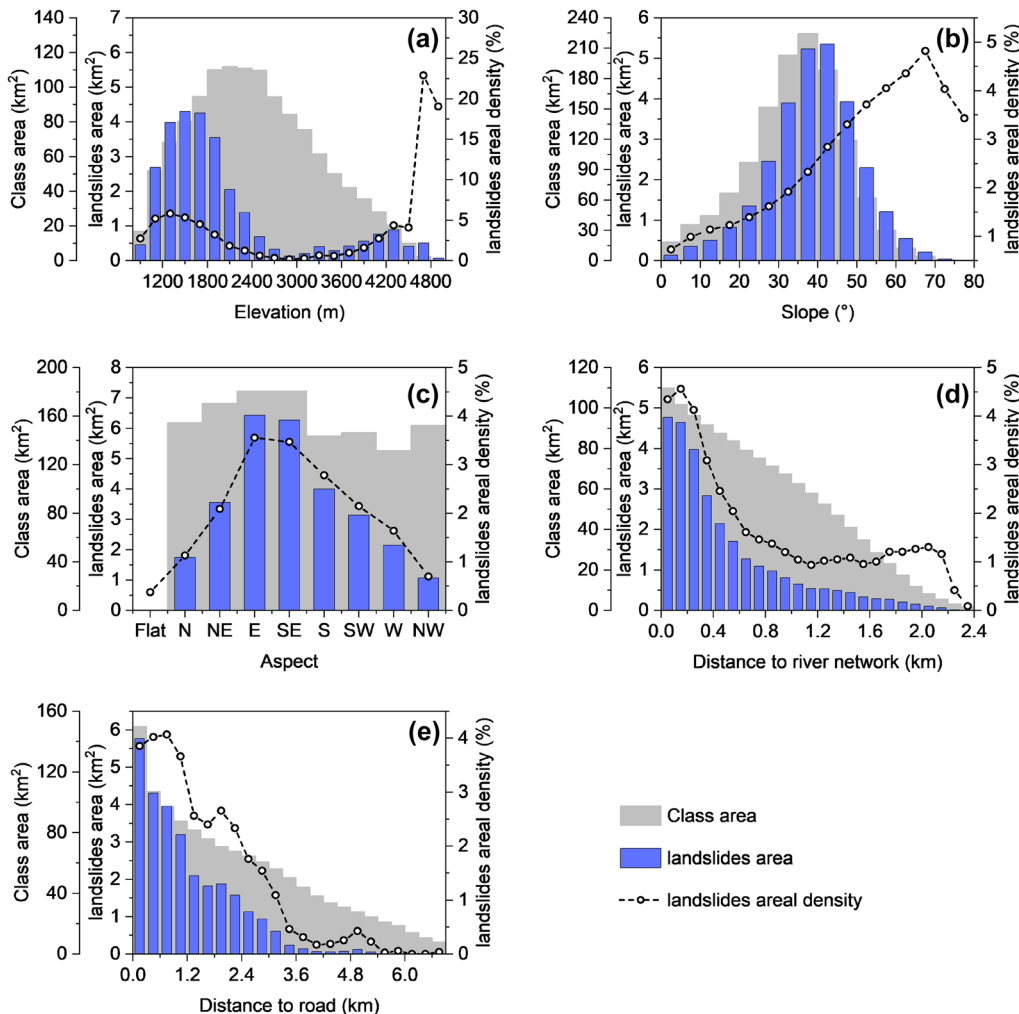


**Fig. 11** Relationship between coseismic landslides distribution and topographic factors: elevation (a), slope (b), aspect (c), distance to river network (d), and distance to road (e)

conversion. We adopted the attribute with the major occupation as the final result of the pixel.

The results reveal that acidic plutonic rocks and mixed sedimentary rocks are the dominant lithologies, covering 52.2% and 25.4% of the total earthquake-affected area, respectively (Fig. 12). The coseismic landslides are also most widely distributed in these two lithologies, with areas of  $15.7 \text{ km}^2$  and  $6.4 \text{ km}^2$ , together accounting for 77.5% of the total landslide area. The remaining components, which are sorted by coverage, are siliciclastic sedimentary rocks (9.3%), basic volcanic rocks (5.1%), metamorphic rocks (4.8%), carbonate sedimentary rocks (1.9%), basic plutonic rocks (0.7%), and pyroclastics (0.6%). Among them, the siliciclastic sedimentary rocks have the largest landslide area ( $3.1 \text{ km}^2$ ), followed by basic plutonic rocks ( $1.2 \text{ km}^2$ ) and carbonate sedimentary rocks ( $1.1 \text{ km}^2$ ). Although coseismic landslides are mainly distributed in acid plutonic rocks and mixed sedimentary rocks, the landslide areal density of any of these two lithologies is not the highest due to their wide distribution in the study area. On the contrary, the basic plutonic rocks exhibit the highest landslide areal density (13.3%). However, it only contributes 0.7% of the study area. Similarly, carbonate sedimentary rocks are the lithology with the second largest landslide areal density (4.9%).

### Discussion

#### Location of the Luding earthquake-triggered landslides

Landslide-generating events counter and influence uplift by mobilizing and redistributing mass and are known to shape different portions of the landscapes unevenly. For a strong earthquake event, a ridgeline is often considered an area with high coseismic landslide density. Due to the effect of micro-landforms, specific parts of the hillslope will be firstly destroyed by external forces such as earthquakes (Fan et al. 2018; Meunier et al. 2008). The area, number density, and relative location of all the landslides triggered by the Luding earthquake along the slopes were plotted on the virtual slope profile (Fig. 13a). We evaluated  $1.0 \text{ km}^2$  as the contributing area threshold of fluvial channels and extracted the relative

landslide locations by measuring the distance of both the highest and lowest point of individual landslide areas to the nearest ridgeline and channel separately. Therefore, a marker close to the origin of the axes indicates a landslide that covers a large proportion of the slope. Conversely, a marker close to the surface indicates a small proportion of slope coverage. Figure 13a shows that a few landslides in the Luding earthquake are triggered in the ridgeline, whereas a large number of small-sized landslides (with an area up to  $1000 \text{ m}^2$ ) are concentrated in the lower section of the slope (with a distance to the valley less than 0.5) and quite close to the foot of slope (with a distance to the stream less than 0.2). Meanwhile, the amount of failures to the whole or most of the slope is small (the regions that are inwards close to the coordinate axis appear low-density blue). This particular distribution pattern, we suspect, is related to the strength of the ground motion. Seismic shake is not strong enough to trigger landslides close to the ridge. To validate this hypothesis, we made the virtual slope profiles based on the graded distribution of PGA (Fig. 13b-d). Combined with the analysis of the landslide area in various PGA distribution (Fig. 10d), it can be concluded that the weak ground motion ( $\text{PGA} < 0.6 \text{ g}$ ) mainly triggered extensive small sizes at the foot of the slope (with a distance to the stream less than 0.2) (Fig. 15c, d). Conversely, strong ground motion not only resulted in a concentration of slope foot but also induced the landslides in a higher slope body (with a distance to the stream higher than 0.5) (Fig. 15b). On the other hand, the higher density of landslides in the foot portion of the slopes might be due to the interaction between river incision, lateral sediment supply (unstable fluvioglacial deposits near Moxi platform) (Fig. 9b), and interference of anthropogenic road rehabilitation.

#### Comparison of landslide area and quantity

By statistical analysis of the global earthquake dataset, linear relationship is usually displayed between the total area and amount of coseismic landslides and earthquake magnitude (Fig. 14a) (Fan et al. 2019). However, the 2022 Luding earthquake-triggered landslides indicate a larger total area compared to the 2013 Lushan earthquake ( $20.1 \text{ km}^2$ ) and the 2017 Jiuzhaigou earthquake ( $10.5 \text{ km}^2$ ). In terms of quantity, the landslide amount of the 2022 Luding earthquake is also greater than that of the 2017 Jiuzhaigou earthquake (1883) and the 2022 Lushan earthquake (1228) (Fig. 14b) (Fan et al. 2018; Zhao et al. 2022). These results suggest the characteristic of large scale and quantity of coseismic landslide triggered by the 2022 Luding earthquake.

The seismogenic fault of the 2008 Wenchuan earthquake is a thrust fault with obvious surface rupture, whereas the seismogenic fault of 2017 Jiuzhaigou earthquake and the 2022 Luding earthquake are both slip-strike faults. It is important to take different fault activity mechanisms into account when analyzing the spatial distribution of coseismic landslides. Through statistics of the three earthquake-triggered landslides, the curve of the 2022 Luding earthquake is similar to others: with the increase of the landslide area, the landslide frequency increases first and then decreases (Fig. 15). In more detail, the distributions of medium and large landslide areas follow an inverse power law, whereas smaller landslides diverge and form a rollover, in which the frequency peaks of different events correspond to different area scales (Fan et al. 2019).

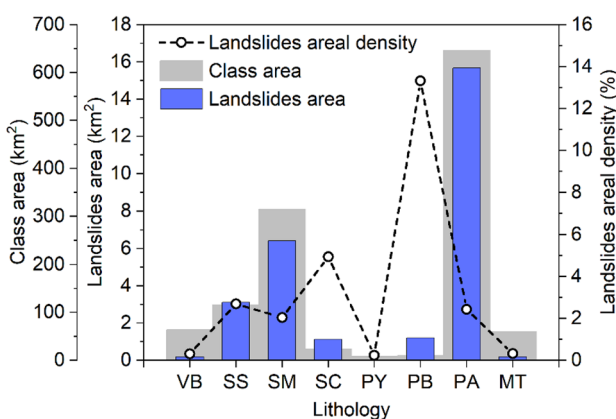
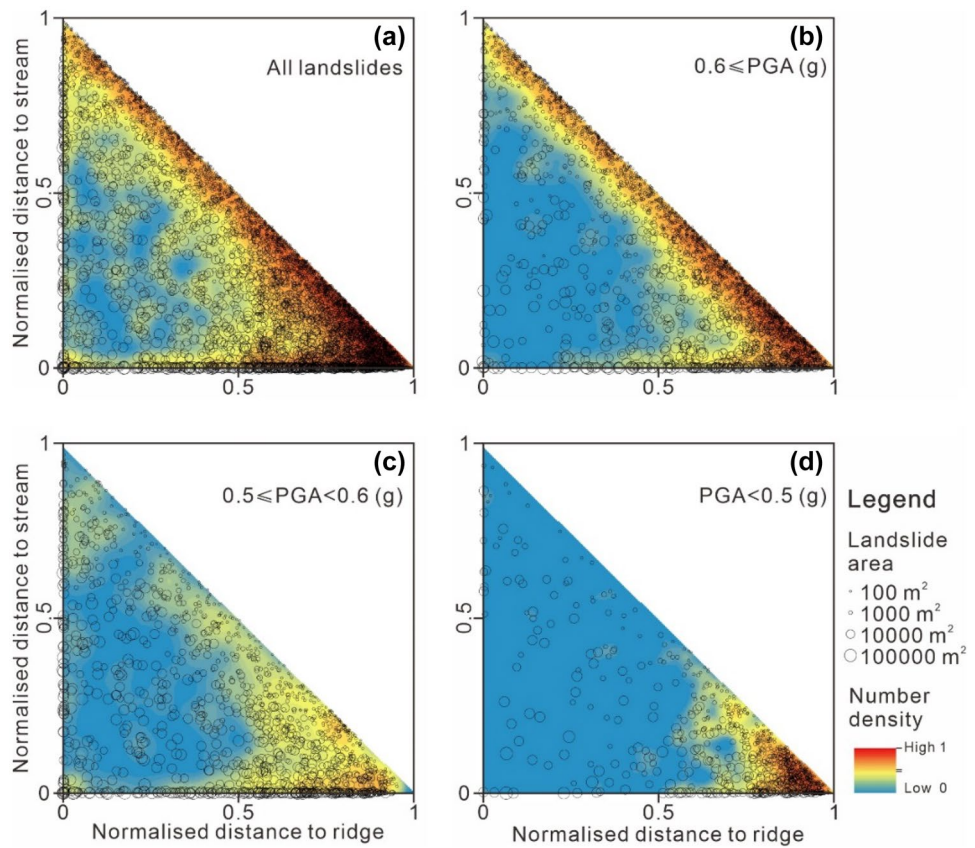


**Fig. 12** Distribution of coseismic landslides in different lithologies. VB: basic volcanic rocks; SS: siliciclastic sedimentary rocks; SM: mixed sedimentary rocks; SC: carbonate sedimentary rocks; PY: pyroclastics; PB: basic plutonic rocks; PA: acid plutonic rocks; MT: metamorphic rocks

**Fig. 13** Virtual slope representation showing the coseismic landslide distribution in different portions of the slope.

**a** All landslides triggered by the Luding earthquake; **b** landslides in the range of PGA greater than 0.6 g; **c** 0.5 to 0.6 g; and **d** less than 0.5 g. The marker size is proportional to the logarithm of the landslide area, and the background color represents the relative landslide number density



It can be concluded that the area of a single landslide triggered by the 2022 Luding earthquake concentrates between 20 and 400 m<sup>2</sup>, whereas they mainly are distributed in 1000–3000 m<sup>2</sup> and 30–500 m<sup>2</sup> in the 2008 Wenchuan earthquake and the 2017 Jiuzhaigou earthquake, respectively. Therefore, the individual coseismic landslide in the 2022 Luding earthquake displays another characteristic of small size compared to the 2008 Wenchuan earthquake and the 2017 Jiuzhaigou earthquake.

The landslides induced by the 2017 Jiuzhaigou earthquake and 2022 Luding earthquake are most small- and medium-sized. In contrast, a significant number of large-sized landslides were triggered

with millions of square meters in the 2008 Wenchuan earthquake, resulting in more than 800 landslide dam barrier lakes (Huang and Fan 2013; Li et al. 2016; Xu et al. 2014). The former two earthquakes are both slip-strike faults with blind fault identification, which generally results in small and scattered landslides. In addition, the approximately symmetric distribution of coseismic landslides along the seismogenic fault implies the characteristics of this focal mechanism (Fan et al. 2018; Gorum et al. 2014). More specifically, the amount of small-sized coseismic landslides in the 2022 Luding earthquake is more than that in the 2017 Jiuzhaigou earthquake. This reason may be attributed to the fact that the 2022 Luding earthquake

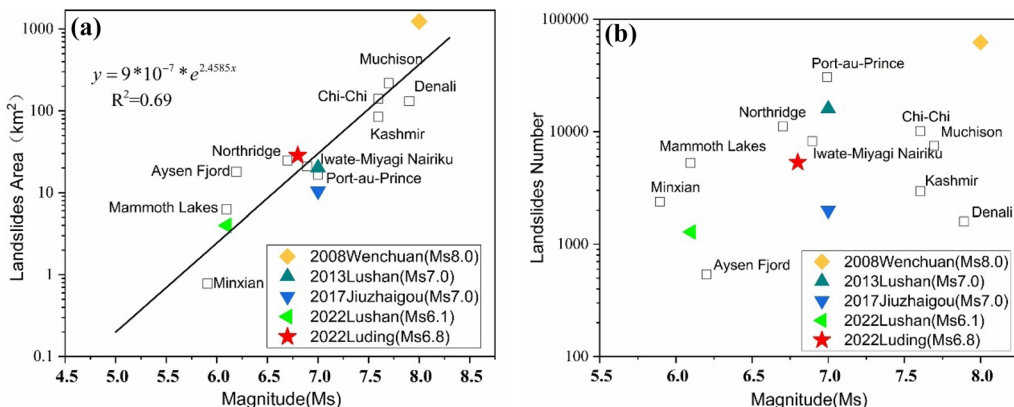


**Fig. 14** Overall coseismic landslide comparison between different earthquakes in **a** area and **b** quantity

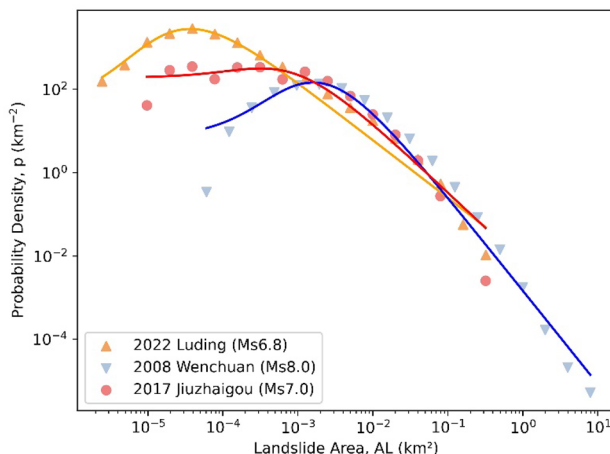


**Fig. 15** Comparison of individual landslide areas in different earthquakes

is located at the Y-shaped junction of the three major faults with active tectonic activity and fragmentized rock mass breakage. In addition, the lithology of the 2022 Luding earthquake-affected area is mainly granite, which is harder than the limestone in the 2017 Jiuzhaigou earthquake-affected region. Therefore, the probability of inducing medium- and large-sized landslides is smaller than that of the 2017 Jiuzhaigou earthquake. In addition, with the development and support of higher-resolution satellite- and UAV-based images, the interpretation of small-scale landslides is more sufficient and accurate, significantly improving the fitting performance.

## Conclusion

In this paper, we proposed a comprehensive workflow to investigate the coseismic landslides triggered by the 2022 Ms6.8 Luding earthquake. We first estimated the coseismic landslides through the prediction model immediately after the earthquake, grasping the overall condition of the induced geological hazards. With the acquisition of multi-source remote sensing images, the detailed coseismic landslide inventory was achieved by combining artificial intelligence algorithms and visual inspection. In total, 5336 landslides were finally recognized up till now, with an area of 28.53 km<sup>2</sup>.

The coseismic landslide obviously developed on both sides of the river and road close to the seismogenic fault. Their elevation, slope, and aspect are concentrated in 1000–2400 m, 25–55°, and E and SE. The main lithology of the induced landslide is acid plutonic rocks, followed by mixed sedimentary rocks and siliceous sedimentary rocks. Compared to the other earthquakes in southwestern China, the total coseismic landslide area is larger, but the individual scale is smaller, which is the most significant characteristic of this event. In more detail, extensive shallow landslides at the foot of slopes are induced, which might be resulted from the river incision, lateral sediment supply, and anthropogenic interferences with medium and low ground shaking in these regions by the Luding earthquake. In the future, we will further explore the controlling

factors behind this development pattern and its profound impact on the long-term evolution of the geological environment.

## Acknowledgements

We thank the Sichuan Bureau of Surveying, Mapping and Geographic Information, Chengdu Jouav Automation Tech Co., Ltd., and Wuhan Dida Information Engineering Co., LTD., for providing satellite- and UAV-based remote sensing images. We also thank the Sichuan Earthquake Administration for providing the seismic intensity and PGA maps.

## Funding

This research is financially supported by the National Science Fund for Distinguished Young Scholars of China (Grant No.42125702), the Tencent Foundation through the XPLORER PRIZE (Grant No.XPLORER-2022-1012), and the Natural Science Foundation of Sichuan Province (Grant No. 2022NSFC0003).

## Declarations

**Conflict of interests** The authors declare no competing interests.

## References

- An Y, Wang D, Ma Q, Xu Y, Li Y, Zhang Y, Liu Z, Huang C, Su J, Li J, Li M, Chen W, Wan Z, Kang D, Wang B (2022) Preliminary report of the 5 September 2022 MS 6.8 Luding earthquake, Sichuan, China. *Earthq Res Adv*. <https://doi.org/10.1016/j.eqrea.2022.100184>
- Bai M, Chevalier ML, Leloup PH, Li H, Pan J, Replumaz A, Wang S, Li K, Wu Q, Liu F (2021) Spatial slip rate distribution along the SE Xianshuihe fault, eastern Tibet, and earthquake hazard assessment. *Tectonics* 40:e2021TC006985
- Bai M, Chevalier M-L, Pan J, Replumaz A, Leloup PH, Métois M, Li H (2018) Southeastward increase of the late Quaternary slip-rate of the Xianshuihe fault, eastern Tibet. Geodynamic and seismic hazard implications. *Earth Planet Sci Lett* 485:19–31
- Bao H, Ampuero J-P, Meng L, Fielding EJ, Liang C, Milliner CW, Feng T, Huang H (2019) Early and persistent supershear rupture of the 2018 magnitude 7.5 Palu earthquake. *Nat Geosci* 12:200–205
- Belgiu M, Drăguț L (2016) Random forest in remote sensing: a review of applications and future directions. *ISPRS J Photogramm Remote Sens* 114:24–31
- Benediktsson JA, Palmason JA, Sveinsson JR (2005) Classification of hyperspectral data from urban areas based on extended morphological profiles. *IEEE Trans Geosci Remote Sens* 43:480–491
- Brenning A (2005) Spatial prediction models for landslide hazards: review, comparison and evaluation. *Nat Hazard* 5:853–862
- Budimir M, Atkinson P, Lewis H (2014) Earthquake-and-landslide events are associated with more fatalities than earthquakes alone. *Nat Hazards* 72:895–914
- Budimir M, Atkinson P, Lewis H (2015) A systematic review of landslide probability mapping using logistic regression. *Landslides* 12:419–436
- Chen G, Xu X, Wen X, Chen YG (2016) Late Quaternary slip-rates and slip partitioning on the southeastern Xianshuihe fault system, eastern Tibetan Plateau. *Acta Geologica Sinica-English Edition* 90:537–554
- Crippen R, Buckley S, Belz E, Gurrola E, Hensley S, Kobrick M, Lavalle M, Martin J, Neumann M, Nguyen Q (2016) NASADEM global elevation model: methods and progress. *The International Archives of the Photogrammetry, Remote Sensing and Spatial Information Sciences* 41:125–128

- Dalla Mura M, Benediktsson JA, Chanussot J, Bruzzone L (2011) The evolution of the morphological profile: from panchromatic to hyperspectral images. *Optical Remote Sens* 123–146. Springer
- Dosovitskiy A, Beyer L, Kolesnikov A, Weissenborn D, Zhai X, Unterthiner T, Dehghani M, Minderer M, Heigold G, Gelly S (2020) An image is worth 16x16 words: transformers for image recognition at scale. arXiv preprint [arXiv:2010.11929](https://arxiv.org/abs/2010.11929)
- Fang S (2023) Prediction-model-of-coseismic-landslides: <https://github.com/fshutong/Prediction-model-of-coseismiclandslides.git>. Accessed 31 Mar 2023
- Fan X, Fang C, Dai L, Wang X, Luo Y, Wei T, Wang Y (2022) Near real time prediction of spatial distribution probability of earthquake-induced landslides—Take the Lushan Earthquake on June 1, 2022 as an example. *J Eng Geol* 30:729–739. <https://doi.org/10.13544/j.cnki.jeg.2022-0328>
- Fan X, Scaringi G, Korup O, West AJ, van Westen CJ, Tanyas H, Hovius N, Hales TC, Jibson RW, Allstadt KE (2019) Earthquake-induced chains of geologic hazards: patterns, mechanisms, and impacts. *Rev Geophys* 57:421–503
- Fan X, Scaringi G, Xu Q, Zhan W, Dai L, Li Y, Pei X, Yang Q, Huang R (2018) Coseismic landslides triggered by the 8th August 2017 Ms 7.0 Jiuzhaigou earthquake (Sichuan, China): factors controlling their spatial distribution and implications for the seismogenic blind fault identification. *Landslides* 15:967–983
- Fan X, Yunus AP, Scaringi G, Catani F, Siva Subramanian S, Xu Q, Huang R (2021) Rapidly evolving controls of landslides after a strong earthquake and implications for hazard assessments. *Geophys Res Lett* 48:e2020GL090509
- Galli M, Ardizzone F, Cardinali M, Guzzetti F, Reichenbach P (2008) Comparing landslide inventory maps. *Geomorphology* 94:268–289
- Gorum T, Korup O, van Westen CJ, van der Meijde M, Xu C, van der Meer FD (2014) Why so few? Landslides triggered by the 2002 Denali earthquake, Alaska. *Quatern Sci Rev* 95:80–94
- Guzzetti F, Mondini AC, Cardinali M, Fiorucci F, Santangelo M, Chang K-T (2012) Landslide inventory maps: new tools for an old problem. *Earth Sci Rev* 112:42–66
- Guzzetti F, Reichenbach P, Ardizzone F, Cardinali M, Galli M (2006) Estimating the quality of landslide susceptibility models. *Geomorphology* 81:166–184
- Hartmann J, Moosdorff N (2012) The new global lithological map database GLiM: a representation of rock properties at the Earth surface. *Geochem Geophys Geosyst* 13
- Hovius N, Stark CP, Allen PA (1997) Sediment flux from a mountain belt derived by landslide mapping. *Geology* 25:231–234
- Huang R, Fan X (2013) The landslide story. *Nat Geosci* 6:325–326
- Keefer DK (1984) Landslides caused by earthquakes. *Geol Soc Am Bull* 95:406–421
- Keefer DK (2000) Statistical analysis of an earthquake-induced landslide distribution—the 1989 Loma Prieta, California event. *Eng Geol* 58:231–249
- Kincey ME, Rosser NJ, Robinson TR, Densmore AL, Shrestha R, Pujara DS, Owen KJ, Williams JG, Swirad ZM (2021) Evolution of coseismic and post-seismic landsliding after the 2015 Mw 7.8 Gorkha earthquake, Nepal. *J Geophys Res: Earth Surf* 126:e2020JF005803
- Lee C-T, Huang C-C, Lee J-F, Pan K-L, Lin M-L, Dong J-J (2008) Statistical approach to earthquake-induced landslide susceptibility. *Eng Geol* 100:43–58
- Lee S (2005) Application of logistic regression model and its validation for landslide susceptibility mapping using GIS and remote sensing data. *Int J Remote Sens* 26:1477–1491
- Li G, West AJ, Densmore AL, Hammond DE, Jin Z, Zhang F, Wang J, Hilton RG (2016) Connectivity of earthquake-triggered landslides with the fluvial network: implications for landslide sediment transport after the 2008 Wenchuan earthquake. *J Geophys Res Earth Surf* 121:703–724
- Liu Y, Chu L, Chen G et al (2021) Paddleseg: a high-efficient development toolkit for image segmentation. arXiv preprint [arXiv:2101.06175](https://arxiv.org/abs/2101.06175)
- Loshchilov I, Hutter F (2017) Decoupled weight decay regularization. arXiv preprint [arXiv:1711.05101](https://arxiv.org/abs/1711.05101)
- Lyu M, Xie J, Ukonmaanaho L, Jiang M, Li Y, Chen Y, Yang Z, Zhou Y, Lin W, Yang Y (2017) Land use change exerts a strong impact on deep soil C stabilization in subtropical forests. *J Soils Sediments* 17(9):2305–2317
- Mantovani F, Soeters R, Van Westen C (1996) Remote sensing techniques for landslide studies and hazard zonation in Europe. *Geomorphology* 15:213–225
- Meunier P, Hovius N, Haines JA (2008) Topographic site effects and the location of earthquake induced landslides. *Earth Planet Sci Lett* 275:221–232
- Ministry of Emergency Management releases intensity map of Luding magnitude 6.8 earthquake in Sichuan Province - Ministry of Emergency Management, PRC. [www.mem.gov.cn/xw/yjglbgzdt/202209/t20220911\\_422190.shtml](http://www.mem.gov.cn/xw/yjglbgzdt/202209/t20220911_422190.shtml). Accessed 31 Mar 2023.
- Mountakis G, Im J, Ogole C (2011) Support vector machines in remote sensing: a review. *ISPRS J Photogramm Remote Sens* 66:247–259
- Nowicki Jessee M, Hamburger M, Allstadt K, Wald DJ, Robeson S, Tanyas H, Hearne M, Thompson E (2018) A global empirical model for near-real-time assessment of seismically induced landslides. *J Geophys Res Earth Surf* 123:1835–1859
- Reichenbach P, Rossi M, Malamud BD, Mihir M, Guzzetti F (2018) A review of statistically-based landslide susceptibility models. *Earth Sci Rev* 180:60–91
- Rodriguez JJ, Kuncheva LI, Alonso CJ (2006) Rotation forest: a new classifier ensemble method. *IEEE Trans Pattern Anal Mach Intell* 28:1619–1630
- Rossi G, Tanteri L, Tofani V, Vannocci P, Moretti S, Casagli N (2018) Multitemporal UAV surveys for landslide mapping and characterization. *Landslides* 15:1045–1052
- Roy DP, Wulder MA, Loveland TR, Woodcock CE, Allen RG, Anderson MC, Helder D, Irons JR, Johnson DM, Kennedy R (2014) Landsat-8: science and product vision for terrestrial global change research. *Remote Sens Environ* 145:154–172
- Tang C, Zhu J, Qi X, Ding J (2011) Landslides induced by the Wenchuan earthquake and the subsequent strong rainfall event: a case study in the Beichuan area of China. *Eng Geol* 122:22–33
- Tang X, Tu Z, Wang Y, Liu M, Li D, Fan X (2022) Automatic detection of coseismic landslides using a new transformer method. *Remote Sens* 14:2884
- Tanyas H, Rossi M, Alvioli M, van Westen CJ, Marchesini I (2019) A global slope unit-based method for the near real-time prediction of earthquake-induced landslides. *Geomorphology* 327:126–146
- Valagussa A, Marc O, Frattini P, Crosta G (2019) Seismic and geological controls on earthquake-induced landslide size. *Earth Planet Sci Lett* 506:268–281
- Van Westen CJ, Castellanos E, Kuriakose SL (2008) Spatial data for landslide susceptibility, hazard, and vulnerability assessment: an overview. *Eng Geol* 102:112–131
- Wang F, Fan X, Yunus AP, Siva Subramanian S, Alonso-Rodriguez A, Dai L, Xu Q, Huang R (2019) Coseismic landslides triggered by the 2018 Hokkaido, Japan (Mw 6.6), earthquake: spatial distribution, controlling factors, and possible failure mechanism. *Landslides* 16:1551–1566
- Wang X, Fan X, Xu Q, Du P (2022) Change detection-based co-seismic landslide mapping through extended morphological profiles and ensemble strategy. *ISPRS J Photogramm Remote Sens* 187:225–239
- Williams JG, Rosser NJ, Hardy RJ, Brain MJ, Afana AA (2018) Optimising 4-D surface change detection: an approach for capturing rockfall magnitude–frequency. *Earth Surf Dyn* 6:101–119
- Woźniak M, Grana M, Corchado E (2014) A survey of multiple classifier systems as hybrid systems. *Information Fusion* 16:3–17
- Xie E, Wang W, Yu Z, Anandkumar A, Alvarez JM, Luo P (2021) SegFormer: simple and efficient design for semantic segmentation with transformers. *Adv Neural Inf Process Syst* 34:12077–12090
- Xu C, Xu X, Yao X, Dai F (2014) Three (nearly) complete inventories of landslides triggered by the May 12, 2008 Wenchuan Mw 7.9 earthquake of China and their spatial distribution statistical analysis. *Landslides* 11:441–461
- Xu Q, Zhang S, Li W, Van Asch TW (2012) The 13 August 2010 catastrophic debris flows after the 2008 Wenchuan earthquake, China. *Nat Hazard* 12:201–216

## Recent Landslides

- Yin Y, Wang F, Sun P (2009) Landslide hazards triggered by the 2008 Wenchuan earthquake, Sichuan, China. *Landslides* 6:139–152
- Zhao B, Li W, Su L, Wang Y, Wu H (2022) Insights into the landslides triggered by the 2022 Lushan Ms 6.1 earthquake: spatial distribution and controls. *Remote Sens* 14:4365
- Zhou Z-H, Feng J (2019) Deep Forest National Science Review 6:74–86

Springer Nature or its licensor (e.g. a society or other partner) holds exclusive rights to this article under a publishing agreement with the author(s) or other rightsholder(s); author self-archiving of the accepted manuscript version of this article is solely governed by the terms of such publishing agreement and applicable law.

**Lanxin Dai · Xuanmei Fan (✉) · Xin Wang (✉) · Chengyong Fang · Chengbin Zou · Xiaochuan Tang · Zhenlei Wei · Mingyao Xia · Dan Wang · Qiang Xu**

State Key Laboratory of Geohazard Prevention and Geoenvironment Protection, Chengdu University of Technology, 610059 Chengdu, China

**Xuanmei Fan**

Email: fxm\_cdut@qq.com

**Xin Wang**

Email: wangxin@cdut.edu.cn